CHEMISTRY OF MATERIALS
Article
Cite This: Chem. Mater. 2017, 29, 9705-9713
pubs.acs.org/cm

Unveiling a New High-Temperature Ordered Magnetic Phase in ε-Fe_2O_3

José Luis García-Muñoz,[†] Arnau Romaguera,[†] Francois Fauth,[‡] Josep Nogués,[§,∥] and Martí Gich*[,†]

[†]Institut de Ciència de Materials de Barcelona, Campus universitari de Bellaterra, ICMAB-CSIC, Bellaterra, E-08193 Barcelona, Spain
[‡]ALBA Synchrotron Light Facility, Cerdanyola del Vallès, 08290 Barcelona, Spain
[§]Catalan Institute of Nanoscience and Nanotechnology (ICN2), CSIC and The Barcelona Institute of Science and Technology, Campus UAB, Bellaterra, 08193 Barcelona, Spain
[∥]ICREA, Pg. Lluís Companys 23, 08010 Barcelona, Spain

Supporting Information

ABSTRACT: Iron oxides are among the most abundant materials on Earth, and yet there are some of their basic properties which are still not well-established. Here, we present temperature-dependent magnetic, X-ray, and neutron diffraction measurements refuting the current belief that the magnetic ordering temperature of ε-Fe_2O_3 is ∼500 K, i.e., well below that of other iron oxides such as hematite, magnetite, or maghemite. Upon heating from room temperature, the ε-Fe_2O_3 nanoparticles' saturation magnetization undergoes a monotonic decrease while the coercivity and remanence sharply drop, virtually vanishing around ∼500 K. However, above that temperature the hysteresis loops present a nonlinear response with finite coercivity, making evident signs of ferrimagnetic order up to temperatures as high as 850 K (T_{N1}). The neutron diffraction study confirms the presence of ferrimagnetic order well above 500 K with $Pna'2_1'$ magnetic symmetry, but only involving two of the four Fe^{3+} sublattices which are ordered below $T_{N2} \approx 480$ K, and with a reduced net ferromagnetic component, that vanishes at above 850 K. The results unambiguously show the presence of a high-temperature magnetic phase in ε-Fe_2O_3 with a critical temperature of $T_{N1} \sim 850$ K. Importantly, this temperature is similar to the Curie point in other iron oxides, indicating comparable magnetic coupling strengths. The presence of diverse magnetic phases is further supported by the nonmonotonic evolution of the thermal expansion. The existence of a high-temperature ferrimagnetic phase in ε-Fe_2O_3 may open the door to further expand the working range of this multifunctional iron oxide.

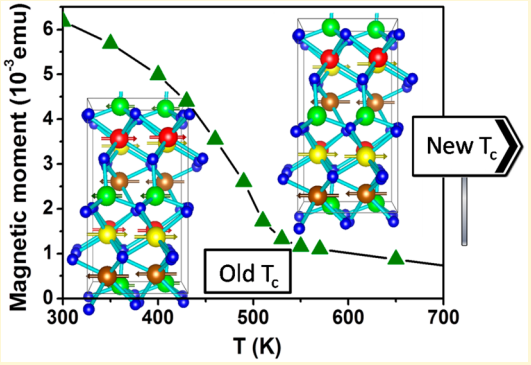

I. INTRODUCTION

Iron oxides constitute an exceptional family of materials that has been studied for many decades, because it presents a fundamental interest and prove a promising applicability for new technologies based on biochemical, magnetic, catalytic, or multiferroic properties.[1−4]

Apart from the amorphous Fe_2O_3, Iron-(III) oxide shows four known polymorph crystal structures: α-Fe_2O_3 (hematite), β-Fe_2O_3 and γ-Fe_2O_3 (maghemite), and ε-Fe_2O_3.[5] While hematite is the most common phase, ε-Fe_2O_3 is the most elusive and one of the less studied polymorphs. This is because its formation requires the mutually exclusive conditions of high temperatures and small sizes.[6−8] The use of sol−gel methods with Si alkoxides and Fe salts made it possible to confine Fe_2O_3 nanoparticles in a silica matrix to prevent their growth while annealing above 1000 °C, allowing, for the first time, acquisition of virtually pure ε-Fe_2O_3, opening the door to the study of this rare polymorph.[9−11] The structural characterization made evident a complex noncentrosymmetric $Pna2_1$ structure isomorphous to the multiferroic $GaFeO_3$, with four Fe sites in the asymmetrical unit, three in octahedral, and one in tetrahedral environments.[8] The magnetic studies revealed an unexpected huge room-temperature coercivity, 20 kOe, making it the transition metal oxide with the highest coercivity and an appealing material for the next-generation high-density magnetic recording media, high-frequency electromagnetic wave absorbers, or a building block for exchange-coupled permanent magnets.[12−15] Moreover, other important functionalities of ε-Fe_2O_3 are related with its magnetoelectric[16] and multiferroic properties.[4] These properties, quite unique among single metal oxides, stem from the structural features specific to this polymorph, in spite of being considered a structural intermediate between α-Fe_2O_3 and γ-Fe_2O_3. Its structure produces a rich temperature-dependent diagram of magnetic phases. Between $T_C = 500$ K and $T_{N2} = 150$ K, ε-Fe_2O_3 exhibits a collinear ferrimagnetic structure due to the antiferromagnetic (AF) coupling (parallel to the a-axis)

Received: August 14, 2017
Revised: October 23, 2017
Published: October 23, 2017

DOI: 10.1021/acs.chemmater.7b03417
Chem. Mater. 2017, 29, 9705−9713

Table 1. Atomic Coordinates of ε-Fe_2O_3 Obtained from SXRPD at 300 and 510 K[a]

	T = 300 K			T = 510 K		
	x	y	z	x	y	z
Fe1	0.1947(5)	0.1497(3)	0.5806(2)	0.1928(6)	0.1499(4)	0.5813(2)
Fe2	0.6828(3)	0.0323(2)	0.7921(3)	0.6823(4)	0.0314(2)	0.7918(3)
Fe3	0.8083(3)	0.1592(2)	0.3062(2)	0.8105(4)	0.1583(2)	0.3079(2)
Fe4	0.1816(5)	0.1538(3)	0.000 00	0.1819(6)	0.1542(4)	0.000 00
O1	0.9754(13)	0.3276(5)	0.4340(5)	0.9739(14)	0.3281(6)	0.4345(6)
O2	0.5112(13)	0.4933(8)	0.4187(9)	0.5030(14)	0.4907(9)	0.4227(13)
O3	0.6537(15)	1.0011(7)	0.1895(5)	0.6533(18)	0.9990(8)	0.1859(5)
O4	0.1624(14)	0.1622(8)	0.1956(4)	0.1614(16)	0.1608(8)	0.1959(4)
O5	0.8449(15)	0.1657(8)	0.6680(5)	0.8450(17)	0.1669(10)	0.6698(5)
O6	0.5286(13)	0.1590(9)	0.9375(6)	0.5386(14)	0.1654(10)	0.9366(7)
cell parameters	a = 5.0967(2)	b = 8.7953(3)	c = 9.4770(3)	a = 5.1133(2)	b = 8.8163(4)	c = 9.4822(4)

[a]Agreement factors for SXRPD pattern at 300 K (510 K): R_B = 1.35 (1.31), R_f = 1.04 (1.01), R_{Mag} = 4.45 (4.48), χ^2 = 4.6 (4.8).

between dissimilar magnetic sublattices. This oxide then presents a broad low-temperature incommensurate magnetic transition starting at 150 K (ICOM1),[17,18] characterized by a large reduction of the coercivity, the remnant, and the saturation magnetization.[17] Under further cooling, below $T_{N3} \approx 85$ K, a second incommensurate magnetic order (ICOM2) takes place.[13] Noticeable anomalies in the dielectric permittivity were reported in conjunction with these two successive transitions.[16] In addition, significant magnetostriction effects were observed in the interval 85−150 K where magnetic changes take place, and spin−lattice coupling brings about atomic shifts within the orthorhombic cell and a nonmonotonous evolution of the Fe−O bonds.[19] A nonzero orbital magnetic moment [$m_L \sim 0.15\ \mu_B$/Fe at room temperature (RT) under 40 kOe] was detected by X-ray magnetic circular dichroism (XMCD) in the hard collinear ferrimagnetic phase ($150 < T < 500$ K), which is suppressed by the magnetostructural changes concurrent with the magnetic transitions within the 85−150 K interval.[15] On cooling, the coercive field drops in that interval from 20 to 0.8 kOe, and then increases again under further cooling in the low-temperature magnetic phase (ICOM2), below 85 K.[14] Likewise, a reentrant behavior of the orbital moment was also monitored by XMCD in the low-temperature magnetic phase.[14] The concurrent magnetostructural changes in the coordination polyhedra around Fe^{3+} sites and the reentrant evolution of the orbital moment should be seen as the signature of a relevant spin−orbit coupling in this magnetoelectric compound. Finally, the RT coexistence of ferrimagnetism and ferroelectricity, albeit with a small magnetocapacitance response, in thin epitaxial films of ε-Fe_2O_3 further highlights the relevance of magnetoelastic couplings in this system, for which possible multiferroic properties in bulk form are still a subject of debate.

Importantly, although the Curie temperature of ε-Fe_2O_3 has been postulated as $T_C \sim 500$ K,[3,11,20−23] no systematic studies of the magnetic properties above this temperature can be found in the literature.

Using diffraction and magnetometry techniques, we have investigated the magnetic and magnetostructural properties of ε-Fe_2O_3 nanoparticles at high temperatures ($T > 500$ K). The results make evident that, contrary to the established scenario, ε-Fe_2O_3 remains ferrimagnetic up to at least T = 850 K, although with a reduced magnetization and a moderate coercivity.

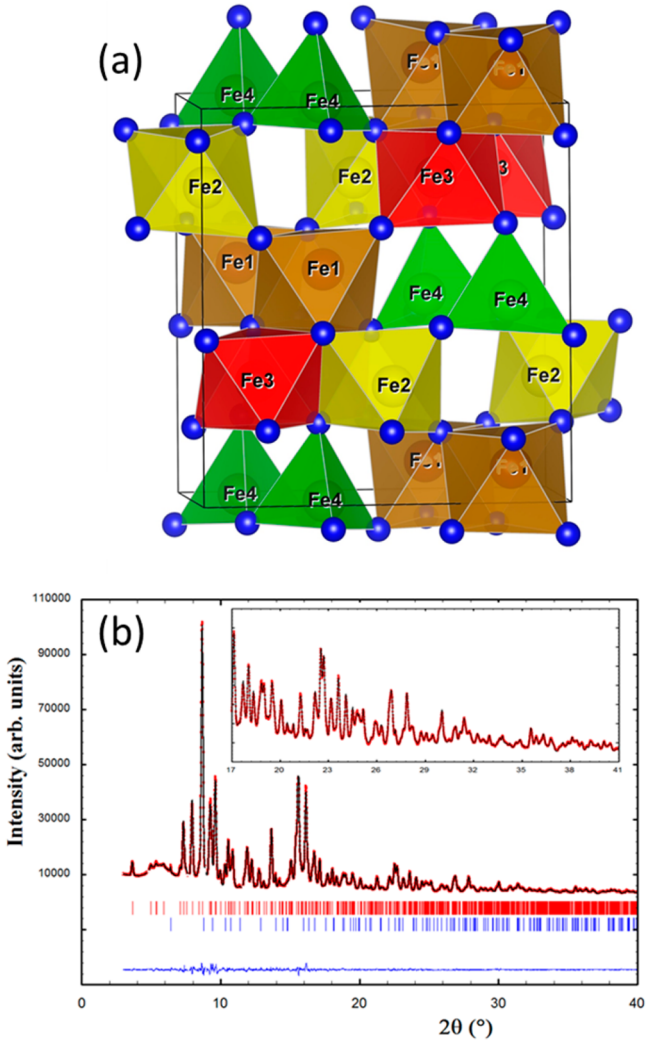

Figure 1. (a) Crystallographic projection of ε-Fe_2O_3. The four crystallographically independent Fe sites are shown with different colors in the structure: Fe1, brown; Fe2, yellow; Fe3, green; Fe4, red). O atoms are represented in dark blue. (b) Rietveld refinement (black solid line) of the synchrotron X-ray pattern of ε-Fe_2O_3 collected at 300 K (red circles, experimental points; bottom blue line, difference). The top row of bars (in red) corresponds to ε-Fe_2O_3, while the bottom row (in blue) is for hematite (α-Fe_2O_3, 2% weight). The inset shows an enlarged view of the high-angle region.

DOI: 10.1021/acs.chemmater.7b03417
Chem. Mater. 2017, 29, 9705−9713

II. EXPERIMENTAL DETAILS

In order to have a good signal-to-noise ratio in neutron diffraction studies, it is desirable to perform measurements using more than 1.5 g of ε-Fe_2O_3 (ideally obtained in a single synthesis). Thus, we prepared a silica gel containing 28 wt % Fe_2O_3 from a hydroethanolic sol of tetraethyl orthosilicate (TEOS) of molar composition TEOS/ethanol/water = 1:5:6 containing dissolved iron nitrate nonahydrate. First, 5.4 mL of Milli-Q water and 26 mL of absolute ethanol (Panreac) were added to a 100 mL beaker and stirred for 5 min. Then, the 10.60 g of iron nitrate (Aldrich) was dissolved and the solution attained a pH ∼ 0.35. Finally, 20 mL of TEOS (Aldrich) was added dropwise to the solution under stirring (∼200 rpm). The stirring, with the beaker covered, was maintained for 20 min after adding the TEOS. The sol was then distributed in 6 cm diameter Petri dishes, attaining a level of 2−4 mm, which were placed in a plastic box, closed with its cover but not hermetically sealed, and placed in a chemical hood at 23 °C. Gelation took place in about 2 weeks. The gels were removed from the Petri dishes, allowed to dry, and subsequently ground in a ceramic mortar to be further dried at 60 °C in a stove. Then, the xerogels were placed in an alumina boat and treated in a tubular furnace in air atmosphere at 200 °C/h to 450 °C and then to 1100 °C at 80 °C/h, and were held for 3 h at this temperature before being cooled to room temperature at 350 °C/h. About 7.5 g of SiO_2/ε-Fe_2O_3 composite was obtained. The resulting material consisted of single crystalline ε-Fe_2O_3 nanoparticles embedded in a silica matrix with an average diameter of around 20 nm as observed by transmission electron microscopy. The silica was etched in hot (80 °C) concentrated NaOH aqueous solution (12 M). For this purpose a round-bottomed flask was filled with 180 mL of distilled water in which 76 g of NaOH was dissolved; then, about 5 g of SiO_2/ε-Fe_2O_3 composite was added to it and stirred overnight on a hot plate set at 80 °C using a water-refrigerated condenser to avoid evaporation of water and a silicone oil bath to maintain a homogeneous temperature around the flask. Then, the suspension was centrifuged at 6000 rpm for 2 min, and the supernatant was discarded. The collected solid was redispersed in water, and the centrifugation was repeated twice. Finally, the tubes used for centrifugation were placed in a stove at 60 °C, and about 1.5 g of ε-Fe_2O_3 nanoparticles was collected after drying.

The quality of the samples was assessed by transmission electron microscopy, magnetic measurements, and X-ray diffraction, as reported earlier.[6,17] Synchrotron X-ray powder diffraction (SXRPD) patterns were collected at the BL04-MSPD beamline[24] of the ALBA Synchrotron Light Facility (Barcelona, Spain) using λ = 0.412 84(6) Å. Patterns were recorded every 90 s by the MYTHEN position-sensitive detector while the sample was warmed from 300 up to 923 K at a rate of 3 K/min. The working temperature was set using a CYBERSTAR hot-air blower. Neutron powder diffraction (NPD) patterns were collected using the high-intensity, high-resolution D2B diffractometer of the Institute Laue-Langevin (ILL, Grenoble, France), between room temperature (RT) and 850 K (λ = 1.594 Å). Structural and magnetic Rietveld refinements were carried out using the Fullprof program.[25] Crystallographic tools from the Bilbao Crystallographic server[26−28] and ISOTROPY software suite[29] were also used.

The magnetic characterization, using dc and ac magnetic fields, was performed with the as-prepared ε-Fe_2O_3 nanoparticles embedded in SiO_2, using a superconducting quantum interferometer device (SQUID) and a vibrating sample magnetometer (VSM) in a physical properties measuring system (PPMS) both from Quantum Design. For the VSM measurements, the ε-Fe_2O_3/SiO_2 material was mixed with a high-temperature alumina cement. The use of ε-Fe_2O_3/SiO_2 composite instead of ε-Fe_2O_3 was necessary to avoid the transformation of ε-Fe_2O_3 to magnetite due to high temperatures and the vacuum environment during the measurements. The ac-susceptibility measurements were performed at 30 Hz and 1 kHz with a magnetic field amplitude of 4 Oe from 300 to 750 K. The temperature dependence of the magnetization, M, was studied after zero-field-cooled (ZFC) and field-cooled (FC) conditions under a dc field of 1 kOe from 300 to 900 K. Hysteresis loops were obtained between 900 and 300 K with a maximum applied magnetic field of 70 kOe.

III. RESULTS AND DISCUSSION

First, it is worth emphasizing that the orthorhombic $Pna2_1$ structure was stable up to the highest temperature reached (923 K). Namely, no transition to other more stable iron oxides (e.g., α-Fe_2O_3 or γ-Fe_2O_3) has been observed up to that temperature.

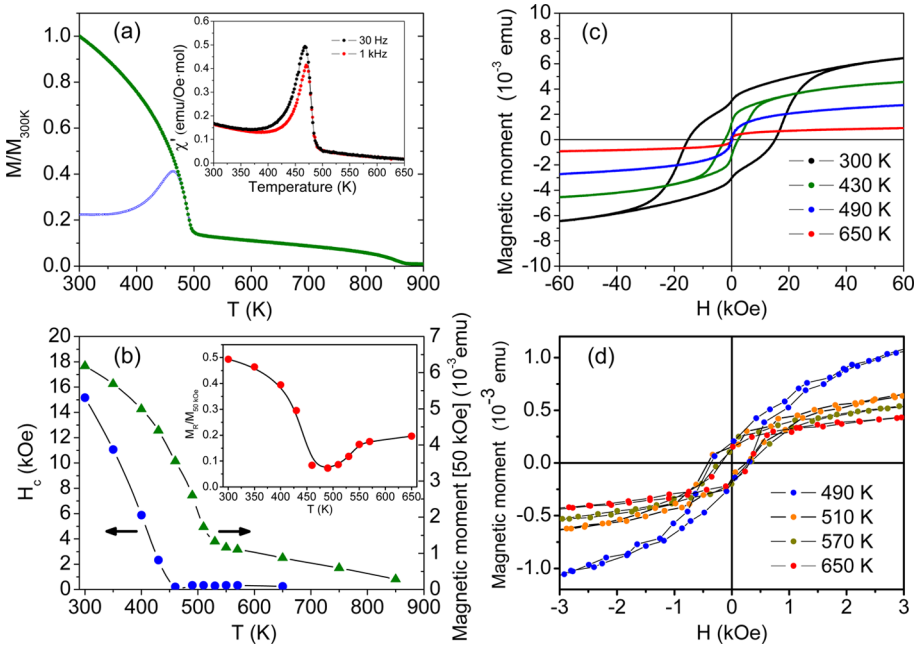

Figure 2. (a) FC (green) and ZFC (blue) dc magnetization curves (1 kOe) of the ε-Fe_2O_3 nanoparticles embedded in SiO_2 between 300 and 900 K. Inset: real part of the ac susceptibility (h = 4 Oe). (b) Temperature evolution of the coercive field (H_C, left axis) and net magnetic moment at 50 kOe (M[50 kOe], right axis). Inset: dependence of the M_R/M[50 kOe] ratio. Hysteresis loops characteristic of (c) the FM2 phase and (d) the FM1 phase (note the different x- and y-scales in both figures, and the loops at 490 and 650 K included in both panels for the sake of comparison).

DOI: 10.1021/acs.chemmater.7b03417
Chem. Mater. 2017, 29, 9705−9713

The structural parameters of ε-Fe_2O_3 and agreement factors from the refinement of SXRPD patterns obtained at 305 and 510 K can be seen in Table 1. Figure 1a displays a projection of the ε-Fe_2O_3 noncentrosymmetric $Pna2_1$ structure, composed of four different Fe sites in the asymmetrical unit cell, three octahedral, and one tetrahedral environments. The coordination octahedra $Fe1O_6$ and $Fe2O_6$ are largely distorted; $Fe3O_6$ is a regular octahedron, and $Fe4O_4$ is the tetrahedron. For clarity we will use the Fe1d, Fe2d, Fe3r, and Fe4t atomic labels where d, r, and t refer to distorted, regular, and tetrahedral polyhedral coordination, respectively.

The presence of a very small minority of impurities was carefully explored by a detailed examination of high-intensity synchrotron patterns. We detected a 2.3(9)% in weight of α-Fe_2O_3 (hematite) as an impurity phase in our nanograin ceramic samples of ε-Fe_2O_3 (corresponding to the bottom row of bars in the refined synchrotron pattern shown in Figure 1b). This corresponds to 0.7 wt % in the SiO_2/Fe_2O_3 composite used for magnetic measurements.

III.a. Magnetometry. The temperature dependence of the ZFC and FC magnetization of the ε-Fe_2O_3 particles embedded in SiO_2 is plotted in Figure 2a. Two ferrimagnetic regimes with very different magnetic behavior can be clearly distinguished below and above ~500 K (denoted FM2 and FM1, respectively). Remarkably, contrary to the scenario assumed in previous reports, the ferrimagnetic FM2 phase does not become paramagnetic above 500 K. The $M(T)$ evolution in Figure 2 reveals a second phase transition, making evident the existence of a new ferrimagnetic state (FM1) between 500 and ~850 K. The transition temperature between FM1 and FM2 can be established at T_{N2} = 480 K by the lambda-shaped peak in the ac susceptibility versus temperature curve presented in the inset of Figure 2a. From the hysteresis loops at T > 500 K it can be clearly seen that FM1 presents a ferromagnetic behavior with finite net magnetic moment and coercivity, H_C.

However, as can be seen in Figure 2b, there is a drastic collapse of the large H_C (characteristic of FM2) and M[50 kOe] at T_{N2} = 480 K (see Figure 2b,c). Moreover, upon heating, M[50 kOe] undergoes a Brillouin-type monotonic decrease up to 550 K, although the coercivity (and remanence, M_r) sharply drops well before this temperature, having practically vanished around ~480 K. Nevertheless, although H_C shrinks by more than a factor of 10 from H_C ~ 16 kOe at RT, it remains moderate (~400 Oe) even at $T \gg$ 500 K (T_{N2}; see Figure 2d). Importantly, from the evolution of the magnetic properties it can be established that the critical temperature of the FM1 phase is about T_{N1} ~ 850 K. Hence, although there is a drastic breakdown of the hard ferrimagnetic state at T_{N2} = 480 K, it does not give rise to a paramagnetic phase, but it is transformed into a new softer ferrimagnetic state.

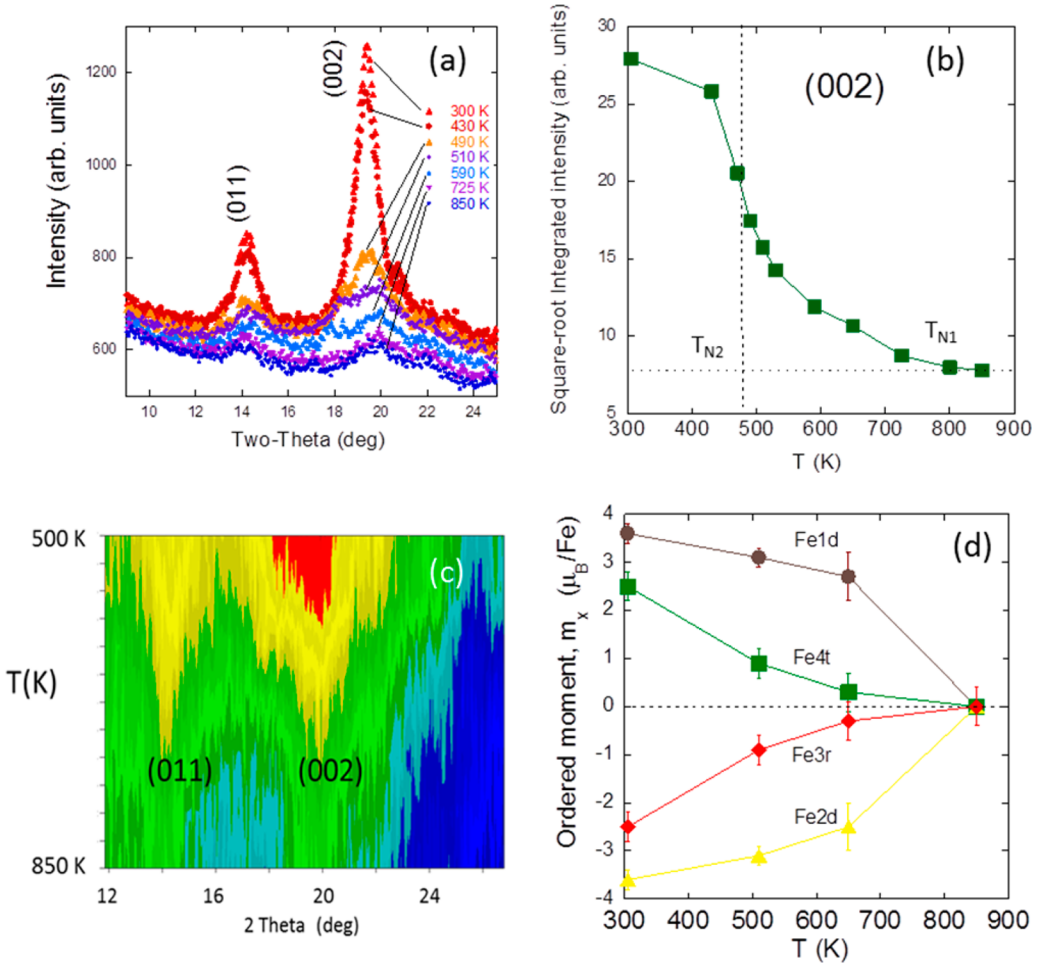

Figure 3. (a) Neutron patterns at selected temperatures in the range composed of the main magnetic peaks (011) and (002). (b) Square-root of the neutron-integrated intensity of the strongest magnetic reflection (002). (c) Evolution of the neutron diffraction intensities above T_{N2} for the characteristic magnetic reflections. (d) Temperature evolution of the ordered magnetic moments refined at Fe1d (brown), Fe2d (yellow), Fe3r (red), and Fe4t (green) sites in the structure.

DOI: 10.1021/acs.chemmater.7b03417
Chem. Mater. 2017, 29, 9705−9713

III.b. Neutron Diffraction Study of the Successive Ferrimagnetic Phases. For a better understanding of the nature of the very high-temperature ferrimagnetic phase, a systematic NPD study was performed.

As can be seen in Figure 3a, the intensity of the magnetic peaks (011) and (002) progressively decreases as the temperature is increased from RT to 850 K. In agreement with the magnetization results, the intensity of the magnetic peaks remains finite even far above T_{N2}. However, the temperature dependence of the integrated intensity of the (002) peak (proportional to the ordered moment), shown in Figure 3b, strongly differs from a Brillouin-type evolution and exhibits the shape of a long magnetic tail that persists far beyond T_{N2}.

The magnetic structures and atomic ordered moments were fully analyzed using the neutron diffraction patterns at the two selected temperatures 305 and 510 K. The former being representative of the ferrimagnetic phase FM2, and the latter (above but close to T_{N2} = 480 K) of the new ferrimagnetic phase FM1. Note that the magnetic reflections detected between T_{N2} (480 K) and T_{N1} (~850 K) do not indicate changes in the extinction conditions or the translational symmetry.

Possible magnetic or Shubnikov space groups compatible with the $Pna2_1$ symmetry and null magnetic propagation vector **k** = 0 were considered. It was found that the magnetic ordering adopts the same magnetic space group in the two ferrimagnetic phases, $Pna'2_1'$ [33.147, transformation to standard settings: (**a**, **b**, **c**; 0, 0, 0)].[25,27] The Rietveld refinement of neutron patterns at 305 K (FM2 magnetic phase) and 510 K (FM1 magnetic phase) is plotted in Figure 4, and the results are summarized in Table 2.

Interestingly, despite the abrupt drop in the displayed magnetization at T_{N2}, there are ordered magnetic moments with very large m_x components that steadily persist in the interval T_{N2} (480 K) < T < T_{N1} (850 K) (m, magnetic moment). Nevertheless, they are found selectively in Fe1d and Fe2d octahedral sites. These two Fe positions are magnetically robust and persist antiferromagnetically coupled above T_{N2}. Their antiparallel ordered moments as refined at intermediate temperatures have been plotted in Figure 3d. Remarkably, the main difference detected between FM2 and FM1 orders concerns the high degree of magnetic disorder at the Fe3rO6 and Fe4tO4 sites. Neutron data did not allow us to discern ordered moments at Fe3r and Fe4t sites independently, and their moments were kept (above T_{N2}) identical and antiparallel, forcing m_x[Fe3r] = $-m_x$[Fe4t], in the neutron refinements. The refined m_x moments at these positions are also displayed in Figure 3d, which shows the evolution of the ordered moments (m_x's)

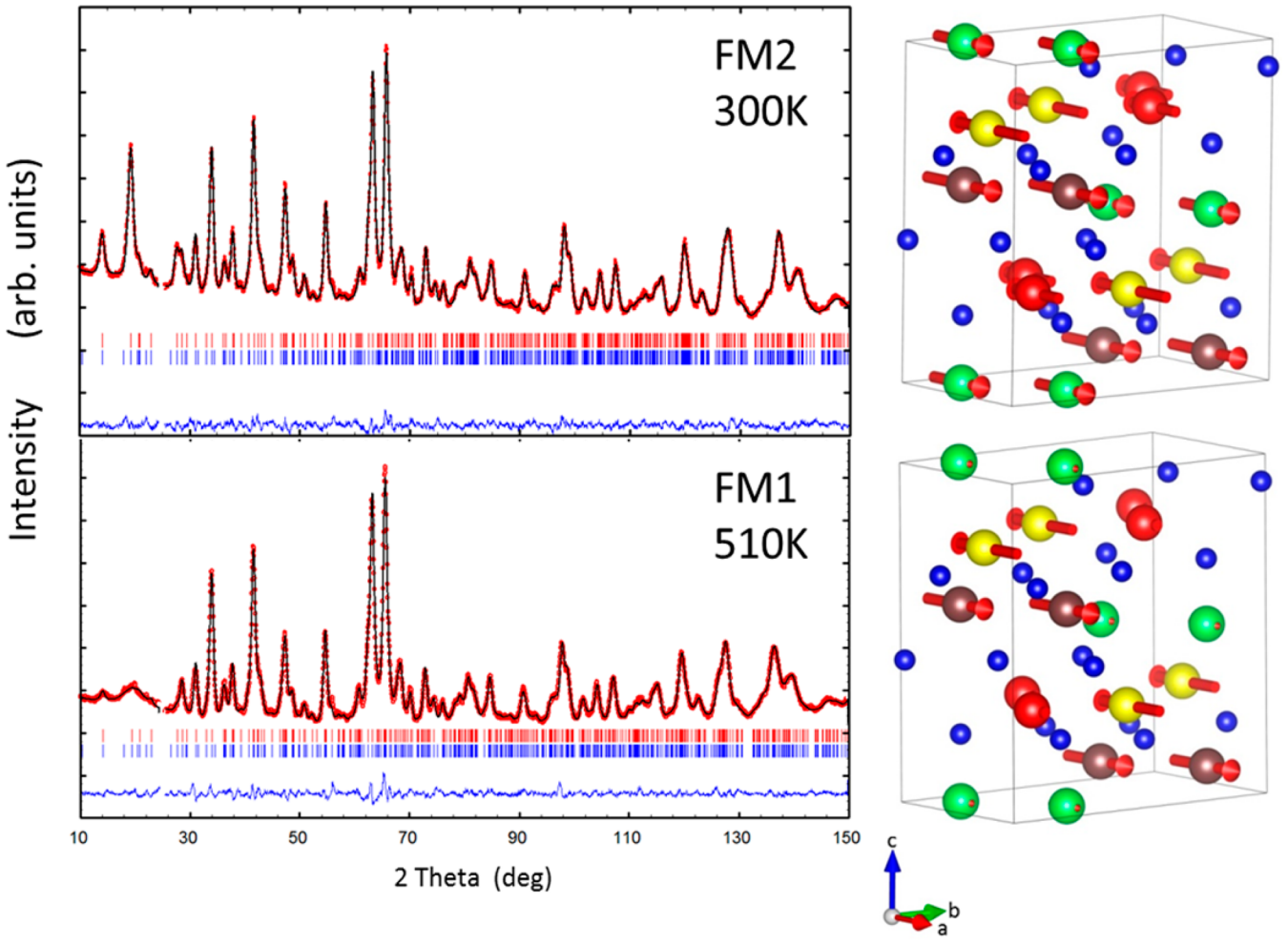

Figure 4. Neutron Rietveld refinement (black line) of the NPD patterns for ε-Fe_2O_3 obtained at 305 K (T < T_{N2}, FM2 ordering) and 510 K (T_{N2} < T < T_{N1}, FM1 ordering) (D2B, red circles, experimental points; bottom blue line, difference). The upper row of reflections correspond to the $Pna2_1$ structure, the lower one to the magnetic ordered phase ($Pna'2_1'$). Goodness factors at 305 K (510 K): R_B = 2.2 2.48 (1.8), R_f = 1.3 1.55 (1.1), R_{Mag} = 2.2 2.92 (1.2), χ^2 = 1.27 0.31 (3.5). (Right) Schematic view of the (bottom) FM1 and (top) FM2 magnetic ordering at the same temperatures. Fe1d (brown), Fe2d (yellow), Fe3r (red), Fe4t (green), and O (dark blue).

DOI: 10.1021/acs.chemmater.7b03417
Chem. Mater. 2017, 29, 9705−9713

Table 2. Magnetic Groups and Refined Magnetic Moments in the Ferrimagnetic FM1 (T_{N1}) and FM2 (T_{N2}) phases[a]

Temperature	300 K	510 K
Magnetic Space Group	***Pna'2$_1$'*** (n. 33.147)	***Pna'2$_1$'*** (n. 33.147)
Transformation to standard setting	(**a**, **b**, **c**; 0, 0, 0)	
Fe atoms in the asymmetric unit	Coordinates Expressed in parent Ort. setting: Fe1d ≈(0.193, 0.149, 0.581) Fe2d ≈(0.682, 0.031, 0.792) Fe3r ≈(0.809, 0.158, 0.307) Fe4t ≈(0.181, 0.153, 0.000)	
Magnetic phase	**FM2**	**FM1**
Refined moments	m$_x$[**Fe1d**]= 3.6(1) μ_B/Fe m$_x$[**Fe2d**]= -3.6(1) μ_B/Fe m$_x$[**Fe3r**]= -2.5(1) μ_B/Fe m$_x$[**Fe4t**]= 2.7(3) μ_B/Fe	m$_x$[**Fe1d**]= 3.1(1) μ_B/Fe m$_x$[**Fe2d**]= -3.1(1) μ_B/Fe m$_x$[**Fe3r**]= -0.9(2) μ_B/Fe m$_x$[**Fe4t**]= 0.9(3) μ_B/Fe
Magnetic structure	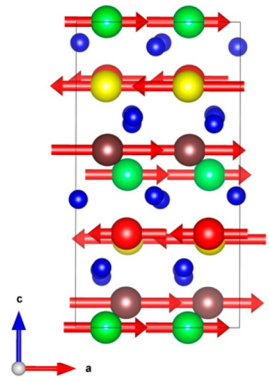	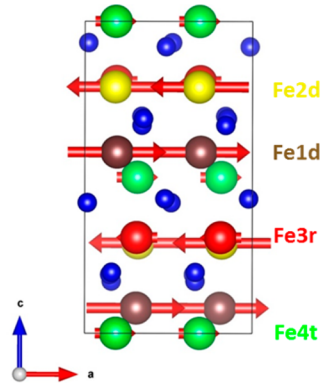

[a]The d, r, and t labels of the four iron sites refer to distorted, regular, and tetrahedral polyhedra, respectively. The goodness factors are given in Figure 3.

refined for the four Fe sites. In the high-temperature phase, the difference between the moments in one antiparallel pair (e.g., Fe3r/Fe4t) is smaller than our experimental error. At RT (305 K), the resultant net uncompensated moment ~0.2 μ_B/Fe (i.e., 14 emu/g) is in agreement with M_s values (net ferromagnetic signal) previously reported.[10,17] Therefore, at the FM2/FM1 (hard/soft) ferrimagnetic phase boundary, there is a clear disruption of the magnetic order of the iron spins occupying the tetrahedral Fe4t and the undistorted octahedral Fe3r sites. The small moment values refined at 510 K indicate that Fe3r and Fe4t sublattices are practically disordered above T_{N2}. Likewise, the onset of magnetic ordering near 850 K is essentially driven by the AFM coupling of Fe spins in the more distorted octahedral positions (Fe1d and Fe2d). Figure 3d clearly illustrates the anomalous evolution of the ordered moments at Fe3r/Fe4t sites. Most likely, this evolution is the result of strong frustration effects between sublattices, which can be identified by the broad magnetic reflections at high temperatures.

Using a molecular-field model, the appearance of spontaneous magnetization in the FM2 phase of ε-Fe_2O_3 has been associated with the lower superexchange $Z_{ij}J_{ij}$ values of the tetrahedral site, compared to those of octahedral sites.[22] As can be seen in Figure 3d the ordered moments at the Fe1d and Fe2d sites are larger than those in the Fe4t tetragonal site in the whole range above room temperature, in concordance with the theoretical predictions. On the other hand, our neutron diffraction results establish that the abrupt enhancement of the magnetization below T_{N2} takes place concurrently with the long-range ordering of Fe4t magnetic atoms occupying the tetrahedral site.

Interestingly, the new ferrimagnetic−paramagnetic boundary is shifted toward the upper characteristic ordering temperatures of ferrimagnetic iron oxides, 950 K for α-Fe_2O_3, 940 K for γ-Fe_2O_3, and 853 K for Fe_3O_4, indicating that ε-Fe_2O_3 presents comparable magnetic coupling strengths. Notably, the NPD analysis unambiguously demonstrates that the ordered magnetic components are associated with ε-Fe_2O_3, ruling out the possibility that the magnetic response above 480 K might be due to impurities of the ferrimagnetic oxides mentioned above, which present a completely different set of magnetic reflections (see Figure S1 in the Supporting Information). Additionally, the fact that some of the magnetic peaks, although very broad, remain finite at 850 K may indicate the possible existence of a frustrated (with no long-range order) ferrimagnetic phase even above T_{N1}, similar to other oxide systems.[30]

III.c. Magnetostructural Coupling at the Ferrimagnetic Transitions Studied Using Synchrotron X-ray Diffraction. Magnetic ordering at high temperatures in ε-Fe_2O_3 concurs with significant magnetostructural and thermal expansion anomalies, as shown by the evolution of the orthorhombic cell obtained from SXRPD (Figure 5). The cell volume reveals

DOI: 10.1021/acs.chemmater.7b03417
Chem. Mater. 2017, 29, 9705−9713

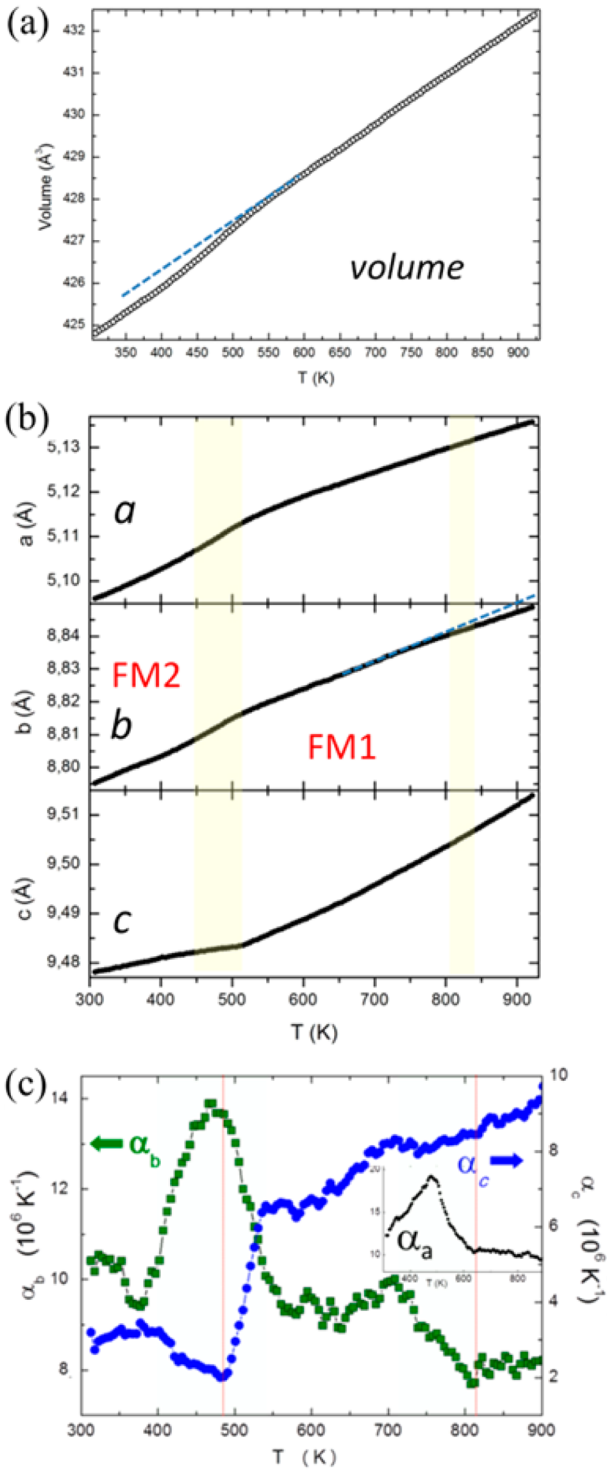

Figure 5. (a) Evolution of the unit-cell volume above room temperature obtained from SXRPD data. (b) Temperature dependence of the orthorhombic cell parameters in the 300−925 K range showing magnetostructural anomalies associated with the emergence of the FM1 and FM2 ferrimagnetic orders. (c) Linear thermal expansion coefficient α_i (i = b and c) derived from SXRPD data and $a_i(T)$ as $\alpha_i = 1/l_{i0} \times dl_i/dT$. The temperature dependence of the coefficients $\alpha_b(T)$ and $\alpha_c(T)$ is shown on the left- and right-axis, respectively. Inset: $\alpha_a(T)$.

an abrupt contraction (≈−0.1%) at about 500 K upon cooling from high temperature (Figure 5a) with the appearance of the hard FM2 phase. The anomaly is also visible in the evolution of all three $a(T)$, $b(T)$, and $c(T)$ cell parameters (Figure 5b): a and b abruptly contract, and c expands when Fe3r and Fe4t spins become long-range ordered (T_{N2}).

In Figure 5c, we plot the linear thermal expansion coefficients α, deduced from $\alpha_i(T)$ as $\alpha_i = 1/l_{i0} \times dl_i/dT$ (l_i: a, b, c), where l_{i0} is the value of the l_i parameter (size of the unit cell along i: a, b, c) at 305 K. Interestingly, there are anomalous contributions to the lattice evolution which are concurrent with the magnetic transitions. On one hand, the most prominent exchange-striction effects come up accompanying the hard/soft ferrimagnetic phase boundary (Figure 2). Similarly, the evolution of $\alpha_b(T)$ in Figure 5c also shows a significant anomaly in the range 700−825 K which could be caused by the appearance of magnetic order at Fe1d and Fe2d sites in the FM1 phase, which is in concordance with the small deviation observed in $b(T)$ near ∼800 K (Figure 5b). Note that the exchange-striction effect at T_{N1} provides further evidence that the magnetic properties between 480 and 850 K do not originate from impurities, but from the FM1 phase of ε-Fe_2O_3.

In this way, although both ferrimagnetic phases exhibit the same magnetic space group [$Pna'2_1'$ (33.147)] and moment orientation (parallel to a), the observed magnetostructural response is very different in both transitions. The origin of these differences should correlate with the dissimilar character of each of the phases (i.e., fully ordered FM2 versus partially frustrated FM1).

IV. CONCLUDING REMARKS

In the preceding sections, we have investigated the puzzling magnetostructural properties of polycrystalline ε-Fe_2O_3 above room temperature. Contrary to the scenario proposed in the literature, magnetic order in this magnetoelectric iron-(III) polymorph does not disappear at the hard-ferrimagnetic transition near 480 K. We have shown that a second ferrimagnetic phase (FM1) persists up to much higher temperatures (near 850 K). The hard ferrimagnetic FM2 phase (holding giant coercivity presumably stimulated by a nonzero orbital angular moment) is transformed to a different ferrimagnet state, FM1, with a much smaller ferromagnetic component and coercivity. Both magnetic orders adopt the magnetic space group $Pna'2_1'$ (33.147), where the main difference between them is the disruption of the magnetic order associated with the Fe3r and Fe4t magnetic atoms. Above 480 K, the iron spins at the sublattices that occupy the regular octahedra, $Fe3O_6$ and $Fe4O_4$ tetrahedra, can hardly keep their antiparallel magnetizations and become rapidly disordered. Consequently, the spontaneous FM magnetization that was sustained by the different magnetic moments in these antiparallel sublattices in FM2 quickly vanishes in FM1. Thus, the small FM component persisting up to $T_{N1} \approx 850$ K results from a slightly dissimilar magnetization at the antiparallel Fe1d and Fe2d sublattices. Hence, we have demonstrated that the ferrimagnetic−paramagnetic phase boundary in ε-Fe_2O_3 is $T_{N1} \sim 850$ K. This temperature is similar to the Curie point in other iron oxides, confirming comparable magnetic coupling strengths. This may open the door to further expand the working range of this multifunctional iron oxide. In fact, these new findings may be an indication that the presumed multiferroic properties of ε-Fe_2O_3 at room temperature actually could persist and extend also into the new ferrimagnetic FM1 phase.

DOI: 10.1021/acs.chemmater.7b03417
Chem. Mater. 2017, 29, 9705−9713

■ ASSOCIATED CONTENT

Supporting Information

The Supporting Information is available free of charge on the ACS Publications website at DOI: 10.1021/acs.chemmater.7b03417.

Simulation of a neutron diffraction pattern of 50 wt % ε-Fe_2O_3 and 50 wt % α-Fe_2O_3 compared to the experimental pattern collected at 305 K (PDF)

■ AUTHOR INFORMATION

ORCID

Josep Nogués: 0000-0003-4616-1371

Martí Gich: 0000-0001-9958-0057

Notes

The authors declare no competing financial interest.

■ ACKNOWLEDGMENTS

We thank, for financial support, the Spanish Ministry of Economy and Competitiveness, through Projects MAT2015-686760-02-2-P, MAT2012-38213-C02-02, and MAT2016-77391-R, and "Severo Ochoa" Programme for Centres of Excellence in R&D (SEV-2015-0496 and SEV-2013-0295). The former projects are cofunded by ERDF of European Union. The Generalitat de Catalunya is also acknowledged for financial support (Projects 2014SGR213 and 2014SGR1015). ICN2 is funded by the CERCA Programme/Generalitat de Catalunya. We also acknowledge ILL and ALBA for granting beam time. C. Ritter is acknowledged for technical assistance during neutron measurements. J.L.G.-M. thanks J. M. Pérez-Mato for fruitful discussions. Ana Arauzo, from the Physical Measurements service at University of Zaragoza is acknowledged for performing ac susceptibility measurements.

■ REFERENCES

(1) Cornell, R. M.; Schwertmann, U. Applications. In *The Iron Oxides*; Wiley-VCH Verlag GmbH & Co. KGaA: Weinheim, Germany, 2004; pp 509−524.

(2) Carraro, G.; Maccato, C.; Gasparotto, A.; Montini, T.; Turner, S.; Lebedev, O. I.; Gombac, V.; Adami, G.; Van Tendeloo, G.; Barreca, D.; Fornasiero, P. Enhanced Hydrogen Production by Photoreforming of Renewable Oxygenates Through Nanostructured Fe_2O_3Polymorphs. *Adv. Funct. Mater.* **2014**, *24*, 372−378.

(3) Tucek, J.; Zboril, R.; Namai, A.; Ohkoshi, S. ε-Fe_2O_3: An Advanced Nanomaterial Exhibiting Giant Coercive Field, Millimeter-Wave Ferromagnetic Resonance, and Magnetoelectric Coupling. *Chem. Mater.* **2010**, *22*, 6483−6505.

(4) Gich, M.; Fina, I.; Morelli, A.; Sánchez, F.; Alexe, M.; Gàzquez, J.; Fontcuberta, J.; Roig, A. Multiferroic Iron Oxide Thin Films at Room Temperature. *Adv. Mater.* **2014**, *26*, 4645−4652.

(5) Zboril, R.; Mashlan, M.; Petridis, D. Iron-(III) oxides from thermal processes-synthesis, structural and magnetic properties, Mossbauer spectroscopy characterization, and applications. *Chem. Mater.* **2002**, *14*, 969−982.

(6) Gich, M.; Roig, A.; Taboada, E.; Molins, E.; Bonafos, C.; Snoeck, E. Stabilization of metastable phases in spatially restricted fields: the case of the Fe_2O_3 polymorphs. *Faraday Discuss.* **2007**, *136*, 345−354.

(7) Sakurai, S.; Namai, A.; Hashimoto, K.; Ohkoshi, S. First Observation of Phase Transformation of All Four Fe_2O_3 Phases (γ -> ε -> β -> α-Phase). *J. Am. Chem. Soc.* **2009**, *131*, 18299−18303.

(8) Tadic, M.; Milosevic, I.; Kralj, S.; Mitric, M.; Makovec, D.; Saboungi, M. L.; Motte, L. Synthesis of metastable hard-magnetic ε-Fe_2O_3 nanoparticles from silica-coated akaganeite nanorods. *Nanoscale* **2017**, *9*, 10579−10584.

(9) Tronc, E.; Chaneac, C.; Jolivet, J. P. Structural and magnetic characterization of e-Fe_2O_3. *J. Solid State Chem.* **1998**, *139*, 93−104.

(10) Jin, B.; Ohkoshi, S.; Hashimoto, K. Giant coercive field of nanometer-sized iron oxide. *Adv. Mater.* **2004**, *16*, 48−51.

(11) Popovici, M.; Gich, M.; Niznansky, D.; Roig, A.; Savii, C.; Casas, L.; Molins, E.; Zaveta, K.; Enache, C.; Sort, J.; de Brion, S.; Chouteau, G.; Nogues, J. Optimized synthesis of the elusive ε-Fe_2O_3 phase via sol-gel chemistry. *Chem. Mater.* **2004**, *16*, 5542−5548.

(12) Namai, A.; Sakurai, S.; Nakajima, M.; Suemoto, T.; Matsumoto, K.; Goto, M.; Sasaki, S.; Ohkoshi, S. Synthesis of an Electromagnetic Wave Absorber for High-Speed Wireless Communication. *J. Am. Chem. Soc.* **2009**, *131*, 1170−1173.

(13) Namai, A.; Yoshikiyo, M.; Yamada, K.; Sakurai, S.; Goto, T.; Yoshida, T.; Miyazaki, T.; Nakajima, M.; Suemoto, T.; Tokoro, H.; Ohkoshi, S. Hard magnetic ferrite with a gigantic coercivity and high frequency millimetre wave rotation. *Nat. Commun.* **2012**, *3*, 1035.

(14) Lopez-Ortega, A.; Estrader, M.; Salazar-Alvarez, G.; Roca, A. G.; Nogues, J. Applications of exchange coupled bi-magnetic hard/soft and soft/hard magnetic core/shell nanoparticles. *Phys. Rep.* **2015**, *553*, 1−32.

(15) Hozumi, T.; Irie, S.; Chiba, T. Magnetic Material, Magnet and Method for Producing the Magnetic Material. Patent WO2012/101752A1, August 2, 2012.

(16) Gich, M.; Frontera, C.; Roig, A.; Fontcuberta, J.; Molins, E.; Bellido, N.; Simon, C.; Fleta, C. Magnetoelectric coupling in ε-Fe_2O_3 nanoparticles. *Nanotechnology* **2006**, *17*, 687−691.

(17) Gich, M.; Roig, A.; Frontera, C.; Molins, E.; Sort, J.; Popovici, M.; Chouteau, G.; Marero, D. M. Y.; Nogues, J. Large coercivity and low-temperature magnetic reorientation in ε-Fe_2O_3 nanoparticles. *J. Appl. Phys.* **2005**, *98*, 044307.

(18) Gich, M.; Frontera, C.; Roig, A.; Taboada, E.; Molins, E.; Rechenberg, H. R.; Ardisson, J. D.; Macedo, W. A. A.; Ritter, C.; Hardy, V.; Sort, J.; Skumryev, V.; Nogues, J. High- and low-temperature crystal and magnetic structures of ε-Fe_2O_3 and their correlation to its magnetic properties. *Chem. Mater.* **2006**, *18*, 3889−3897.

(19) Tseng, Y. C.; Souza-Neto, N. M.; Haskel, D.; Gich, M.; Frontera, C.; Roig, A.; van Veenendaal, M.; Nogues, J. Nonzero orbital moment in high coercivity ε-Fe_2O_3 and low-temperature collapse of the magnetocrystalline anisotropy. *Phys. Rev. B: Condens. Matter Mater. Phys.* **2009**, *79*, 094404.

(20) Forestier, H.; Guiot-Guillain, G. A new ferromagnetic variety of iron sesquioxide. *C. R. Hebd. Seances Acad. Sci.* **1934**, *199*, 720−723.

(21) Schrader, R.; Buttner, G. A New phase of Iron (III)-oxide - ε-Fe_2O_3. *Z. Anorg. Allg. Chem.* **1963**, *320*, 220−234.

(22) Ohkoshi, S.; Namai, A.; Sakurai, S. The Origin of Ferromagnetism in ε-Fe_2O_3 and ε-$GaxFe_{2-x}O_3$ Nanomagnets. *J. Phys. Chem. C* **2009**, *113*, 11235−11238.

(23) López-Sánchez, J.; Serrano, A.; Del Campo, A.; Abuín, M.; Rodríguez de la Fuente, O.; Carmona, N. Sol−Gel Synthesis and Micro-Raman Characterization of ε-Fe_2O_3 Micro- and Nanoparticles. *Chem. Mater.* **2016**, *28*, 511−518.

(24) Fauth, F.; Boer, R.; Gil-Ortiz, F.; Popescu, C.; Vallcorba, O.; Peral, I.; Fullà, D.; Benach, J.; Juanhuix, J. The crystallography stations at the Alba synchrotron. *Eur. Phys. J. Plus* **2015**, *130*, 160.

(25) Rodriguez-Carvajal, J. Recent Advances in Magnetic-Structure Determination by Neutron Powder Diffraction. *Phys. B* **1993**, *192*, 55−69.

(26) Aroyo, M. I.; Perez-Mato, J. M.; Capillas, C.; Kroumova, E.; Ivantchev, S.; Madariaga, G.; Kirov, A.; Wondratschek, H. Bilbao crystallographic server: I. Databases and crystallographic computing programs. *Z. Kristallogr. - Cryst. Mater.* **2006**, *221*, 15−27.

(27) Aroyo, M. I.; Kirov, A.; Capillas, C.; Perez-Mato, J. M.; Wondratschek, H. Bilbao crystallographic server. II. Representations of crystallographic point groups and space groups. *Acta Crystallogr., Sect. A: Found. Crystallogr.* **2006**, *62*, 115−128.

(28) Perez-Mato, J. M.; Gallego, S. V.; Tasci, E. S.; Elcoro, L.; de la Flor, G.; Aroyo, M. I. Symmetry-Based Computational Tools for Magnetic Crystallography. *Annu. Rev. Mater. Res.* **2015**, *45*, 217−248.

DOI: 10.1021/acs.chemmater.7b03417
Chem. Mater. 2017, 29, 9705−9713

(29) Campbell, B. J.; Stokes, H. T.; Tanner, D. E.; Hatch, D. M. ISODISPLACE: a web-based tool for exploring structural distortions. *J. Appl. Crystallogr.* **2006**, *39*, 607−614.
(30) Kuriki, A.; Moritomo, Y.; Xu, S.; Ohoyama, K.; Kato, K.; Nakamura, A. Diffuse scattering due to geometrical frustration in Mn_3O_4. *J. Phys. Soc. Jpn.* **2003**, *72*, 458−459.

DOI: 10.1021/acs.chemmater.7b03417
Chem. Mater. 2017, 29, 9705−9713